Article

Corrosion Performance of (TiAlZrTaNb)N$_x$ High-Entropy Nitrides Thin Films Deposited on 304 Stainless Steel via HiPIMS

Maria-Camila Castañeda, Oscar Piamba * and Jhon Olaya

Grupo de Investigación en Corrosión, Tribología y Energía, Departamento de Ingeniería Mecánica y Mecatrónica, Facultad de Ingeniería, Universidad Nacional de Colombia, Bogota 111321, Colombia; mcastanedabe@unal.edu.co (M.-C.C.); jjolayaf@unal.edu.co (J.O.)
* Correspondence: oepiambat@unal.edu.co

Abstract

In this study, the electrochemical corrosion behavior of TiAlZrTaNb nitride thin films deposited on 304 stainless steel substrates was investigated. The thin films were synthesized using high-power impulse magnetron sputtering (HiPIMS) and are classified as high-entropy alloys (HEAs). The microstructure, morphology, and chemical composition of the coatings were characterized by X-ray diffraction (XRD), scanning electron microscopy (SEM), and energy-dispersive X-ray spectroscopy (EDS), respectively. Corrosion resistance was evaluated through electrochemical impedance spectroscopy (EIS) and potentiodynamic polarization tests, employing tap water, acetic acid, and citric acid solutions at room temperature as electrolytes. The results demonstrated that the TiAlZrTaNbN coating exhibits a dense and homogeneous structure with a uniform elemental distribution. XRD analysis revealed the presence of face-centered cubic (FCC) crystalline phases, which significantly contribute to the coating's corrosion resistance. Furthermore, the coating displayed exceptional corrosion performance in both acetic acid and citric acid electrolytes—simulating food environments with a pH $\leq$ 4.5—as revealed by a substantial reduction in corrosion current density and a positive shift in corrosion potential. These findings provide valuable insights into the properties of TiAlZrTaNbN coatings and underscore their potential for enhancing the durability of mechanical components employed in the food industry.

Keywords: high-entropy nitride coating; HEA; TiAlTaZrNbN; corrosion resistance; HiPIMS

1. Introduction

High-entropy alloys (HEAs) have recently attracted significant attention as alternative materials for surface coatings, owing to the unique properties derived from their multi-component compositions and complex structures. These alloys typically comprise five or more elements, each present in atomic percentages ranging from 5% to 35%. This compositional diversity promotes the formation of solid-solution structures, imparting exceptional mechanical properties, thermal stability, high corrosion resistance, and chemical stability in demanding environments [1]. Previous studies on alloys such as (TiHfNbZrTa)N [2], (TiZrNbTaFe)N [3], and (TiZrNbAlYCr)N [4] have demonstrated superior properties compared to traditional alloys. These enhancements are attributed to the synergistic effects of high entropy, sluggish atomic diffusion, lattice distortion, and the so-called cocktail effect [5].

The functionality of these coatings is determined by their intended application, which depends on the constituent elements, the deposition technique employed, and their performance under specific environmental conditions. Additionally, these coatings exhibit high hardness due to the presence of transition metal elements, which contribute to elevated hardness at high temperatures, optimal substrate adhesion, and chemical stability [6–8].

The corrosion and oxidation resistance of HEAs have been extensively investigated, revealing their potential as protective coatings, particularly when they contain elements such as Cr, Co, Ni, Ti, and Mo, which enhance corrosion resistance. The incorporation of Mo improves pitting resistance, whereas elements such as Al, Cu, and Mn may reduce corrosion resistance due to microstructural changes or the formation of undesirable phases. Likewise, the oxidation resistance of HEAs, especially those containing Al, Cr, and Si, is attributed to the formation of dense, protective oxide layers at elevated temperatures, rendering them suitable for high-temperature applications. Studies indicate that HEA coatings can surpass traditional coatings in oxidation resistance, with grain structure, chemical composition, and the presence of specific phases playing critical roles [9].

In high-entropy alloys containing transition metal nitrides, nitrogen content plays a pivotal role in determining the microstructure, as well as the mechanical and anticorrosive properties of the material. Shu et al. reported that, in (TiNbZrTa)N coatings, the presence of nitrogen induces a phase transformation from body-centered cubic (BCC) to a NaCl-type face-centered cubic (FCC) structure, with lattice parameters comparable to those of binary nitrides. These coatings exhibit reduced surface roughness and increased density; a grain morphology analysis further indicates that nitrogen facilitates the synthesis of smoother surfaces with finer grains [10]. However, the corrosion performance of these films, when evaluated in 0.1 M sulfuric acid electrolytes, revealed comparatively lower corrosion resistance for these high-entropy nitrides.

Bachani et al. [3] investigated the corrosion behavior of two high-entropy alloys, [TiZrNbTaFe and (TiZrNbTaFe)N], with varying nitrogen contents, deposited on 304SS, 420SS, and P-type Si (100) substrates in a 35 wt.% NaCl solution. Potentiodynamic polarization measurements demonstrated a broad passivation range (943–1520 mV) for the coated samples, in contrast to 573 mV for the uncoated 304SS substrate. The corrosion current density (I_corr) for the 304SS substrate was approximately 0.211 $\mu A/cm^2$, whereas the TiZrNbTaFeN coating exhibited a significantly lower value of 0.036 $\mu A/cm^2$, indicating enhanced corrosion resistance imparted by the coating. Furthermore, electrochemical impedance spectroscopy (EIS) revealed that the capacitive loop sizes for the coated samples were substantially larger than those of the 304SS substrate, reflecting improved capacitive behavior and greater resistance to charge transfer, which the authors attribute to the dense microstructure of the coatings.

In the physical vapor deposition (PVD) sputtering process, various parameters, including sputtering power, target distance, deposition temperature, and gas pressure, significantly influence the quality and composition of the coatings. The chamber pressure is particularly important, as it affects the particle density by determining the energy of arriving sputtered particles and thereby alters the coating's growth pattern [11]. Advances in plasma deposition processes, such as high-power impulse magnetron sputtering (HiPIMS), have enabled the production of high-quality thin films by increasing the ionization of the deposition flux. HiPIMS typically operates at voltages between 400 and 2000 V and current densities of 0.1–10 A cm^{-2}, utilizing voltage pulses around 50 Hz to achieve high instantaneous power and generate dense plasma [12,13]. The intensified ion bombardment during film growth promotes the development of thin, dense coatings with high hardness and improved adhesion [14]. Coating density is a critical parameter, as it enhances the

coating's effectiveness as a barrier to mass diffusion, thermal exposure, corrosion, and wear [15]

In this study, TiAlZrTaNb nitride thin films were deposited on 304 stainless steel (304SS) substrates using the HiPIMS technique. The coatings will be analyzed to evaluate their compositional, morphological, structural, and microstructural characteristics. Finally, electrochemical corrosion tests will be conducted to assess the coatings' performance in three electrolytes commonly used as test media in the food industry.

2. Materials and Methods

(TiAlZrTaNb)N_x coatings were deposited onto AISI 304 stainless steel substrates using the HiPIMS technique. The deposition system comprised a water-cooled magnetron equipped with a 100 mm diameter target, having an equiatomic chemical composition of 20% Ti, Al, Zr, Ta, and Nb. Plasma generation was achieved using a Hipster Pulser, model 100–200 VAC, (Ionautics, Stockholm, Sweden) in combination with a synchronizer operating at a frequency of 600 Hz and a pulse width of 60 μs. Prior to deposition, a base vacuum pressure of approximately 3.5×10^{-4} Pa was established. The coatings were synthesized at a substrate temperature of 250 °C, a working pressure of 5×10^{-1} Pa, and gas flow rates of 233×10^{-9} m^3/s for argon (Ar) and 33.3×10^{-9} m^3/s for nitrogen (N$_2$). Under the established deposition conditions and with an estimated deposition time of 30 min, 200 nm-thick coatings were deposited. The thicknesses were measured by means of confocal microscopy. Table 1 summarizes the principal deposition parameters used during the fabrication of the coatings.

Table 1. Deposition parameters used for the fabrication of (TiAlZrTaNb)N_x coatings by HiPIMS.

Parameters	Values
Deposition time [min]	30
Frecuency [Hz]	500
Pulse width [μs]	60
N$_2$ flow rate [m^3/s]	33.3×10^{-9}
Ar Flow rate [m^3/s]	233×10^{-9}
Working pressure [10^{-3} mbar]	5.07 ± 0.15
Substrate temperature [°C]	250.43 ± 0.98
Discharge Voltage Udc [V]	628
Discharge current Idc [mA]	302.86 ± 3.44
Peak Power Pavg [W]	190.57 ± 2.57
Peak Current Ipk [A]	13 ± 0.58

The substrates consisted of AISI 304 stainless-steel discs with a diameter of 12.70 mm and a thickness of approximately 2.5 mm. These samples were polished to a mirror-like finish and subsequently cleaned in an ultrasonic bath with acetone and isopropyl alcohol. An additional cleaning step involved etching in the sputtering system at a temperature of up to 250 °C, under a pressure of 2 Pa, with an argon flow rate of 233×10^{-9} m^3/s, and a current intensity of 0.050 A for 10 min.

The structure of the coatings was analyzed by X-ray diffraction (XRD) using a PANalytical X'Pert Pro diffractometer with Cu Kα radiation (λ = 1.54 Å). Crystallite size was estimated based on the average full width at half maximum (FWHM) of the peaks obtained from the reference diffraction pattern. The Voigt function, Gaussian adjustment of the spectrogram, and the Scherrer equation were employed for crystallite size estimation.

The chemical composition of the coating was determined using energy-dispersive X-ray spectroscopy (EDS). The analysis was carried out using a EDS Bruker Nano GmbH (Bruker, Berlin, Germany) probe at a magnification of 500×. The sample morphology

was characterized using a scanning electron microscope (SEM) from Bruker Nano GmbH, operating under vacuum pressures ranging from 4×10^{-2} to 5 Pa, with a working distance of 15 mm and magnifications of 500× and 1000×. An accelerating voltage of 30 kV was applied, and both secondary electron and backscattered electron detectors were utilized. This study was complemented by confocal laser scanning microscopy (CLSM) using a ZEISS LSM 700 (Carl Zeiss, Oberkochen, Germany) microscope. Images were acquired at a magnification of 500× at a minimum of two locations within the area of interest, using a 47 μm pinhole and a 405 nm wavelength laser.

The chemical composition of the coatings was determined using energy-dispersive X-ray spectroscopy (EDS) with a Bruker Nano GmbH probe at a magnification of 500×. Sample morphology was characterized by scanning electron microscopy (SEM) using a Bruker Nano GmbH instrument, operating under vacuum pressures ranging from 4×10^{-2} to 5 Pa, with a working distance of 15 mm and magnifications of 500× and 1000×. An accelerating voltage of 30 kV was applied, and both secondary electron and backscattered electron detectors were utilized. Confocal laser scanning microscopy (CLSM) was performed with a Carl Zeiss microscope, acquiring images at a magnification of 500× at a minimum of two locations within the area of interest using a 47 μm pinhole and a 405 nm wavelength laser. This CLSM was used to measure thickness and roughness.

Electrochemical tests were conducted in three solutions at room temperature, defined as food simulants in accordance with the CoE protocol and the Italian decree [16]. These regulations specify the criteria that materials must meet to be considered suitable for food contact. The solutions used were as follows:

- Acetic acid: 3% (v/v) CH_3COOH solution in distilled water, simulating foods with a pH = 2.5;
- Citric acid: $C_6H_8O_7$ solution at 5 g/L in distilled water, simulating foods with a pH = 2.18;
- Tap water: simulating aqueous, alcoholic, and fatty foods: pH 6.8 ± 0.5; Conductivity 75 μS·cm^{-1}.

Electrochemical tests were performed using a GAMRY 600 (Gamry Instruments, Warminster, PA, American) potentiostat. All samples were stabilized for 40 min inside a Faraday cage prior to each analysis, and data were processed with Gamry Echem Analysis 7.10 software. Potentiodynamic polarization tests were conducted with a starting potential of −0.3 V and a final potential of 1.25 V, at a scan rate of 0.5 mV/s, using a working electrode area of 0.196 cm^2, a reference electrode of calomel, a contra electrode of platinum, and a stabilization time of 40 min. Electrochemical impedance spectroscopy (EIS) measurements were performed at various immersion times (1 h, 24 h, 48 h, 72 h, and 168 h) using an excitation voltage of 10 mV.

3. Results and Discussion

3.1. Elemental Composition

Energy-dispersive X-ray spectroscopy (EDS) was employed to analyze the elemental composition of the TiAlTaZrNbN coating deposited on the AISI 304 substrate via the HiPIMS technique. Measurements were conducted at three distinct points on the sample, and the chemical composition results showed that the nitrogen concentration was 49.2 ± 0.48 at%, and the concentration of five components is reported in both atomic percent (% at.) and weight percent (% wt.) in Table 2.

The coating can be classified as an equiatomic alloy with equimolar proportions, as it contains five principal elements. The compositional variation of each element in this type of deposition generally depends on factors such as sputtering yield, angular distribution, and gas scattering [3]. Although aluminum exhibits the highest sputtering efficiency (1.2) compared to the other target elements [Ta (0.6), Nb (0.6), Zr (0.7), and

Ti (0.6)] [17], it presented a relatively low atomic concentration in the coating (18.24 at.%). This phenomenon may be attributed to the rapid depletion of aluminum at the onset of the process, followed by a decrease in its concentration on the target surface, which limits its availability for deposition and reduces its flux toward the substrate [14]. Additionally, this may be exacerbated by the detachment of aluminum from the synthesized surface, a consequence of its low atomic mass and the bombardment of Ar ions—a phenomenon previously reported in high-entropy alloy nitride films containing aluminum [18].

Table 2. Elemental composition of the TiAlTaZrNbN coating on the AISI 304 substrate.

	Nb	Ti	Zr	Al	Ta	N
Element concentration %at.	11.87 ± 0.46	12.08 ± 0.12	9.70 ± 0.27	8.89 ± 0.19	8.24 ± 0.24	49.24 ± 0.48

By definition, a high-entropy alloy (HEA) must consist of at least five elements, each with an atomic percentage between 5% and 35%. This requirement is satisfied by the TiAlTaZrNbN coating, in which all five elements are considered principal elements, as their atomic percentages exceed 5%. The configurational entropy (ΔS_{conf}) was calculated using Equation (1), and, according to the high-entropy alloy criterion ($\Delta S_{conf} \geq 1.5$ R), the coating meets this classification [19].

$$\Delta S_{conf} = -R\sum_{i=1}^{n} (x_i \ln x_i) = 2.05R \tag{1}$$

For the calculated value of 2.05 R, the high configurational entropy and low Gibbs free energy favor the formation of a solid and thermodynamically stable coating. These conditions are conducive to achieving exceptional properties, including high mechanical strength and hardness, superior wear resistance, thermal stability at elevated temperatures, and enhanced resistance to corrosion and oxidation [20,21]. Table 3 presents a selection of alloys composed of similar elements, along with their corresponding ΔS_{conf} values.

Table 3. Examples of high-entropy alloys with corresponding configurational entropy calculation.

| HEA	ΔS_{conf}	Reference
(TiNbZrTa)N	1.54 R	[22]
(TiZrNbTaFe)N	1.67 R	[2]
(TiZrNbAlYCr)N	1.89 R	[3]

3.2. Microstructure and Morphology

The microstructure and morphology of the deposited coatings were analyzed. Diffractograms of the thin film deposited on the AISI 304 substrate, obtained via X-ray diffraction, are presented in Figure 1. The X-ray diffraction pattern reveals the Bragg reflections of the TiAlTaZrNbN coating on the AISI 304 substrate. On the (111) plane at 2θ positions of $34.28°$ and $34.39°$, and on the (200) plane at $40.70°$ and $41.05°$, it is evident that, for the coating deposited on steel, the peak associated with the (111) plane is sharper and narrower than that of the (200) plane.

The diffraction peaks of the TiAlTaZrNbN coating on the substrate are shifted toward lower diffraction angles compared to those of the TiN structure, as indicated in the figure, which corresponds to an increase in the lattice parameter (0.4466 nm) relative to pure TiN (0.424 nm) [23]. This shift may also indicate the presence of compressive stresses [24]. Furthermore, based on the peak positions, it can be inferred that the coating exhibits a face-centered cubic (FCC) structure of the NaCl type, forming a solid solution phase with crystalline microstructures. This is characteristic of high-entropy alloys, which tend to form single-phase microstructures due to their sluggish diffusion effect [3].
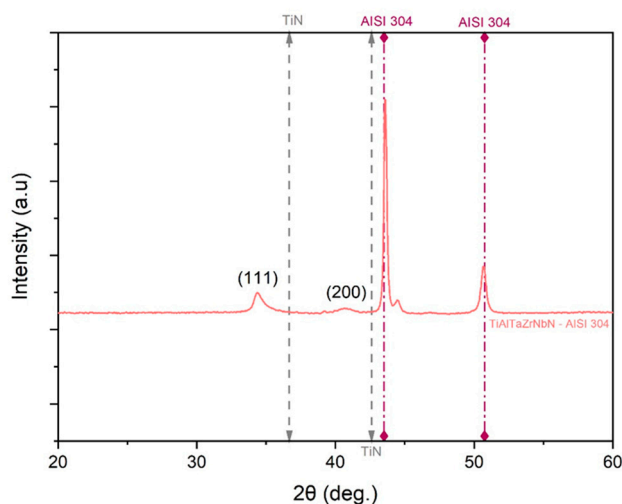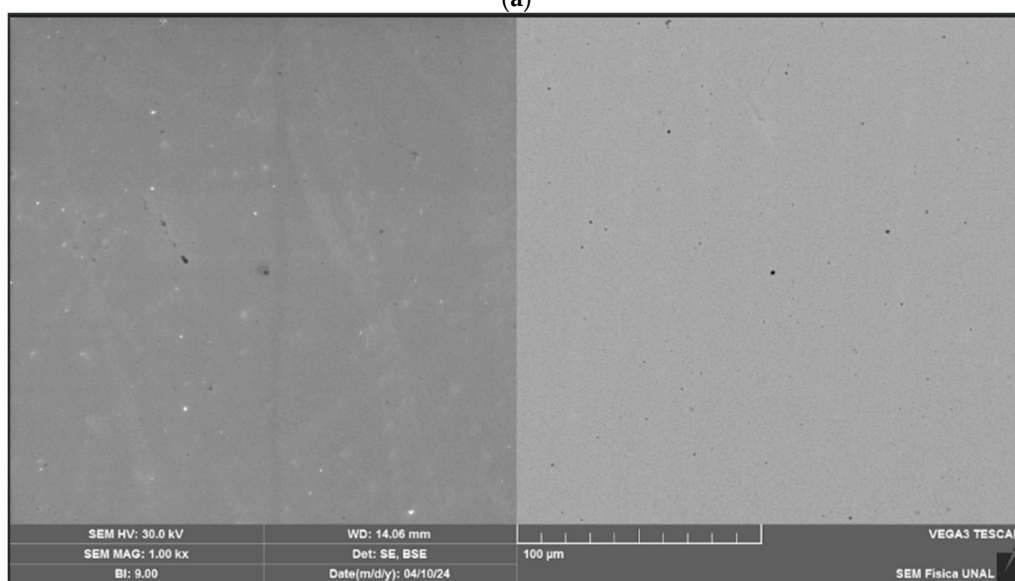
Figure 1. (**a**) X-ray diffractogram for the TiAlTaZrNbN coating, and (**b**) SE and BSE images obtained by SEM magnification 1000× of the TiAlTaZrNbN coating on AISI 304 substrate.

The crystallite size and lattice parameter for the coatings on AISI 304 in the (111) plane were found to be 16.57 nm and 0.4466 nm, respectively. Comparison with other studies reveals similar parameters in other high-entropy nitrides. Specifically, for the (TiZrNbAlYCr)N and (AlCrMoTaTiZr)N films, the crystallite sizes and lattice parameters are 15 nm, 15.74 nm, 0.437 nm, and 0.4288 nm, respectively [4,25]. Additionally, the crystallite size obtained in this study is larger than that reported for the (TiZrNbTaFe)N layer, which ranges from 5.1 to 9.2 nm, with a lattice parameter of 0.4401 nm [3].

The surface of the coating appears smooth and dense, without distinctive features, pores, or roughness, indicating homogeneous agglomeration Figure 1b However, the specific growth pattern of the coating cannot be conclusively determined. Generally, coatings of this nature may exhibit either columnar morphologies or fine-grained microstructures [26]. Figure 1b allows for the observation of a smooth surface, without visible defects onset as pores or fractures, with a measured roughness of 0.049 ± 0.02.

3.3. Corrosion Performance

The corrosion performance of the coating was evaluated by means of an electrochemical test. Figure 2 shows the potentiodynamic polarization curves for both the AISI 304 substrate and the coating deposited on the substrate in various solutions: 3% (*v/v*) acetic acid in distilled water, 5 g/L citric acid in distilled water, and tap water. In Figure 2a, the coating sample exhibits a lower corrosion current density compared to the substrate sample. This suggests that the coating provides improved corrosion resistance to the selected substrate. This behavior can be partially explained by the fact that the high-entropy film possesses an FCC solid solution structure, which typically exhibits better corrosion resistance than stainless steels, as it acts as a diffusion barrier, preventing corrosion caused by ion diffusion [27].
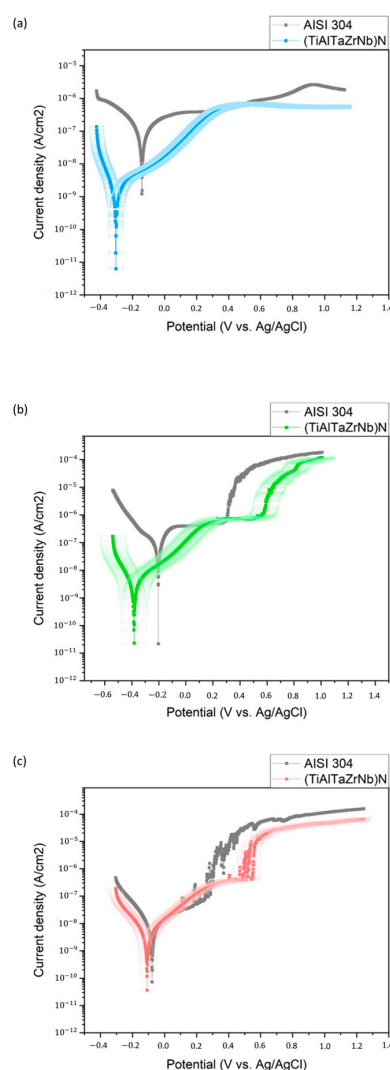

Figure 2. Potentiodynamic polarization curves of the substrate and the (TiAlTaZrNb)N coating; electrolytes: (**a**) acetic acid solution; (**b**) citric acid solution; and (**c**) tap water.

Similarly, the potentiodynamic polarization curves of the AISI 304 substrate and the coating deposited in a 5 g/L citric acid solution provide information about the corrosion behavior (Figure 2b). It can be observed that the coating sample also exhibits a lower corrosion current density in this medium, suggesting that the TiAlTaZrNbN coating provides better corrosion resistance.

In contrast, for the third medium, the curves for the coating and substrate in tap water are shown in Figure 2c. According to the European Protocol, this electrolyte simulates

aqueous, alcoholic, or fatty foods. Both curves show passivation zones; the substrate has lower potential values than the coating. However, both curves exhibited minimal potential differences, suggesting that the corrosion resistance did not vary significantly. The coating, with its slight leftward shift compared to the substrate curve, shows a slightly lower corrosion current density but presents a slightly more negative corrosion potential.

From these curves, the values of corrosion current density (Icorr) and corrosion potential (Ecorr) shown in Table 4.0 were obtained, using the corresponding curve fitting performed with the Gamry Echem Analyst software. The Icorr and Ecorr values obtained for the substrate in acetic acid were 283 nA/cm^2 and −141 mV, respectively, while for the coating, the values were 6.050 nA/cm^2 and −59.20 mV. In the same way, the parameters in the citric acid solution were 472 nA/cm^2 and −205 mV, respectively, while for the coating, they were 5.47 nA/cm^2 and −97.40 mV. These results indicate that a higher Ecorr and a lower Icorr represent better corrosion resistance [27], since a more positive Ecorr value reflects a lower thermodynamic tendency to corrode and a lower Icorr value corresponds to a lower dynamic corrosion rate [28]. Therefore, the corrosion parameters determined for the coated sample demonstrate that the coating acts as an effective barrier between the active surface of the untreated sample and the electrolyte.

Table 4. Results obtained through Tafel fitting in Gamry Echem Analysis for the substrate and the (TiAlTaZrNb)N coating; electrolytes: 3% (v/v) acetic acid, 5 g/L citric acid, and tap water.

Electrolyte	Sample	Icorr (nA/cm^2)	Ecorr (mV)	Corrosion Rate (mpy)	Pitting Potential (mV)
Acetic acid	AISI 304	283.0	−141.0	658.9×10^{-3}	-
	(TiAlTaZrNb)N	6.050	−59.20	14.1×10^{-3}	-
Citric acid	AISI 304	472.0	−205.0	1100×10^{-3}	0.3
	(TiAlTaZrNb)N	5.47	−97.40	12.7×10^{-3}	0.58
Tap water	AISI 304	13.50	−77.6	31.4×10^{-3}	0.3
	(TiAlTaZrNb)N	7.55	−94.80	17.6×10^{-3}	0.5

Additionally, in Figure 2c, it can be observed that both curves exhibit passivation behavior. The protective efficacy of the passive film on the substrate and coating would be related to the integrity and uniformity of the passive film [29]. This was confirmed by the corrosion current density (Icorr) and corrosion potential (Ecorr) values shown in Table 4. The obtained Icorr and Ecorr values for the substrate in tap water were 13.50 nA/cm^2 and −77.6 mV, respectively, while for the coating, the values were 7.55 nA/cm^2 and −94.80 mV.

It is also evident that the corrosion rate found in the acid mediums is lower for the coating compared to that of the steel. Furthermore, using Equation (2), the protection efficiency of the films can be calculated; a protection efficiency of 98.88% was obtained in the acetic medium and 98.80% for the citric medium. Similarly, the corrosion rate in tap water is comparable. Both are on the order of 10^{-3}, although the substrate rate is slightly higher. In this case, the protective performance of the film shows an efficiency of 44.07%.

$$P_i\ (\%) = \left[1 - \left(\frac{I_{corr}}{I_{corr}^0} \right) \right] \times 100 \qquad (2)$$

In addition to this, the coating showed no evident alterations in its structure, such as pores, cracks, or pitting, but instead remained as a homogeneous and dense layer on the substrate. Regarding the EDS chemical composition analysis of the coating before and after the potentiodynamic polarization test, it shows that the atomic percentage of the elements it is composed of does not present significant differences. Complementing this, the roughness

data before and after the corrosion test are presented in Table 5, which confirms that there are no significant changes in the average surface roughness.

Table 5. Roughness data before and after the Tafel analysis in electrolytes: acetic acid, citric acid, and tap water.

Electrolyte	Sample	Pa (µm)	Psk (µm)	Pv (µm)
Acetic acid	Before	0.049 ± 0.02	0.425 ± 0.15	0.079 ± 0.02
	After	0.027 ± 0.001	-0.403 ± 0.12	0.102 ± 0.03
Citric acid	Before	0.028 ± 0.003	$0.296 \pm 0,26$	0.065 ± 0.02
	After	0.024 ± 0.019	$-0.193 \pm 0,37$	0.056 ± 0.09
Tap water	Before	0.032 ± 0.002	$-1.287 \pm 0,92$	0.244 ± 0.09
	After	0.030 ± 0.006	$-0.20 \pm 0,42$	0.101 ± 0.05

Electrochemical impedance spectroscopy (EIS) was employed to evaluate the corrosion behavior and electrochemical mechanisms of both coated and uncoated substrates in a solution, using an equivalent circuit model. Measurements were taken after a 40 min stabilization period at 0, 24, 48, 72, and 168 h. The phase diagram allows for the visualization of the two representative behaviors of the EIS technique, namely the high-frequency region, associated with the capacitive behavior of the coating, and the low-frequency region with a negative slope, which is related to the resistive behavior of the electrolyte.

Initially, as shown in Figure 3a,b, at 0 h and a frequency of 0.01 Hz, the impedance of the substrate is slightly lower than that of the coated sample. At lower frequencies, the coating exhibits a slightly higher impedance compared to the substrate, indicating better resistance to polarization, except in the case of the tap water electrolyte [Figure 3c], where the substrate shows higher impedance values at lower frequencies. Furthermore, the analysis of the graphs over time revealed consistent behavior relative to time 0. Figure 3d shows the electrical equivalent circuit model used to analyze the electrochemical impedance response.

The phase angle and impedance modulus at the initial time (0 h) for the substrate and the coating in the three solutions are presented in Figure 3. After 1 h of immersion, the phase angle at 0.01 Hz is lower for the uncoated substrate than for the coated sample, which exhibits a higher phase angle for the three electrolytes. During this period, the highest phase angle for the substrate was observed in the acetic acid solution at approximately 71.83° (0.5 Hz), in citric acid at 73.17° (0.99 Hz), and in tap water at 75.72° (around 0.79 Hz), while the coating reaches higher values of 79.79°, 79,99° and 76.60°, respectively. Analyzing the overall behavior of the systems, a slight increase in the phase angles associated with the coating is presented, indicating a stable consistency and uniformity of the TiAlTaZrNbN film. Additionally, the coating exhibits a higher phase angle at lower frequencies, highlighting its superior capacitive performance.

The electrochemical impedance spectroscopy (EIS) results obtained for the three electrolytes under investigation were fitted using the simple impedance model in REAP2CPE (Rapid Electrochemical Assessment of PAINT-REAP) within the Gamry Echem Analyst software. This model incorporates the constant phase element (CPE), consisting of three resistors and two constant-phase elements (imperfect capacitors), which enables a more accurate fit to the experimental data. The polarization resistance *(Rp)* was calculated as the sum of the three resistances (Rsol + Rcor + Rpo).

Table 6 presents the parameters derived from the fitted model, allowing for a comparison of the coating and substrate performance in the three solutions. A higher pore resistance (Rpo), observed for the coating in both acetic and citric acid electrolytes at 0 h and 168 h, indicates superior electrochemical stability and corrosion resistance compared

to the substrate. This improvement is attributed to the reduced pore formation within the coating, which limits electrolyte penetration to the metal surface and thereby delays the onset of corrosion. Notably, Rpo is one of the most critical parameters for assessing the chemical stability of coatings in corrosive environments [30].
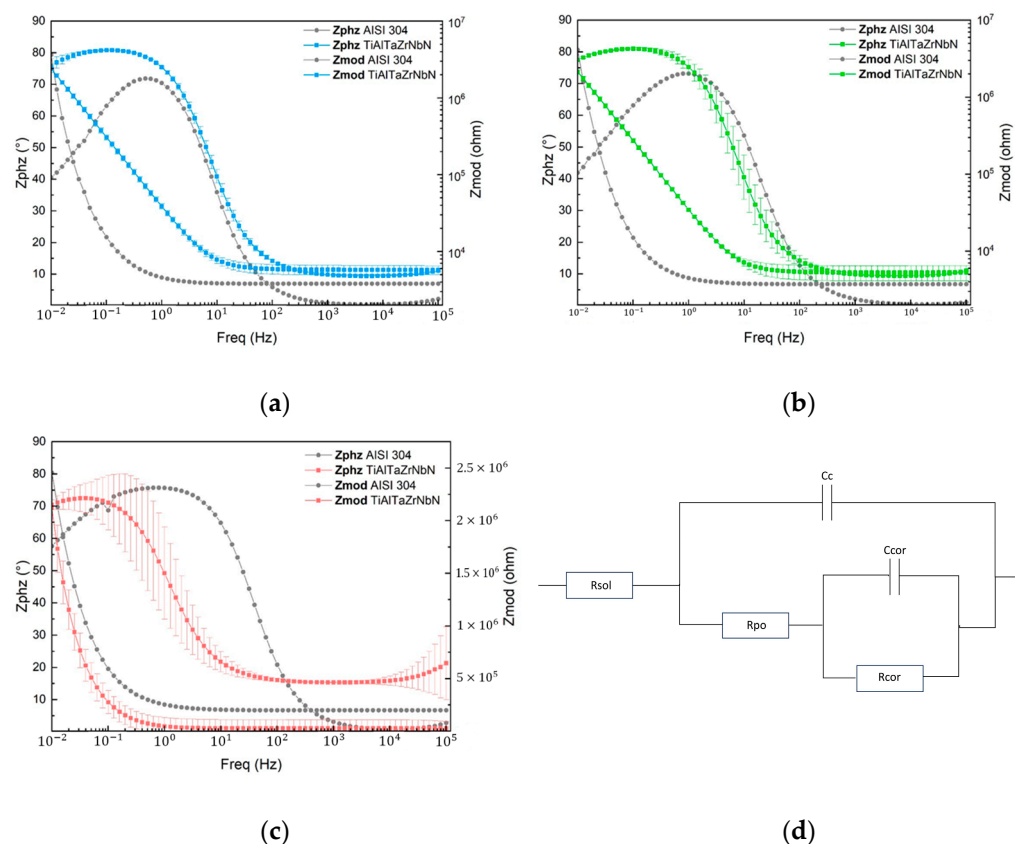

(a)

(b)

(c)

(d)

Figure 3. Phase angle and impedance modulus for AISI 304 substrate and TiAlTaZrNbN coating as a function of frequency in: (**a**) acetic acid solution; (**b**) citric acid solution; (**c**) tap water; and (**d**) Diagram of electrical equivalent circuit model.

Conversely, the capacitance values of both the coating and the substrate are similar, and both decrease gradually over time. This parameter is related to the film's ability to absorb water and its dielectric properties, specifically its capacity to store electrical energy and resist the conduction of an electric current [31]. The observed decrease in capacitance suggests that the porosity of the coating increases over time. As the number of pores grows, the electrolyte can penetrate the coating more readily and potentially reach the substrate.

Furthermore, for the coating in the acetic acid solution, the charge transfer resistance (Rcor) is lower than the pore resistance (Rpo), indicating that electrolyte penetration through the pores of the coating is more difficult than the electrochemical reaction between the substrate and the electrolyte. Additionally, the solution resistance (Rsol) is relatively high, on the order of 10^3 Ω, while the film or coating resistance (Rp) is even higher, on the order of 10^7 Ω. This indicates that both the penetration of the electrolyte through the film and its subsequent reaction with the substrate occur at very slow rates [32].

Moreover, throughout the immersion period, the coating consistently exhibited polarization resistance (Rp) values higher than those of the AISI 304 substrate in acidic media, as shown in Figure 4a,b. This result indicates superior protection against electrolytes and a lower density of defects in the films. These findings are consistent with the results obtained from the potentiodynamic polarization analysis.

Table 6. Fitted EIS parameters for substrate and coating in acetic acid, citric acid, and tap water. Rsol: solution resistance; Rcor: resistance to corrosion; Rpo: pore resistance; Ccor: constant phase element between the coating and the substrate; Cc: constant phase element between the electrolyte to the coating; Rp: polarization resistance.

| Electrolyte—Sample	Time (min)	Rsol (Ω)	Rpo (Ω)	Cc ($S \times s^a$)	m	Rcor (Ω)	Ccor ($S \times s^a$)	n	Rp (Ω)
Acetic acid AISI 304	0	5.5×10^3	7.29×10^5	5.46×10^{-6}	0.89	8.29×10^5	8.30×10^{-6}	0.90	1.56×10^6
	168	5.6×10^3	2.35×10^7	3.80×10^{-6}	0.91	7.18×10^3	1.57×10^{-4}	0.56	2.35×10^7
Acetic acid TiAlTaZ-rNbN	0	4.6×10^3	2.52×10^7	5.58×10^{-6}	0.91	2.78×10^4	1.15×10^{-5}	0.58	2.52×10^7
	168	5.4×10^3	5.59×10^7	3.60×10^{-6}	0.92	8.40×10^4	1.33×10^{-5}	0.58	5.60×10^7
Citric acid AISI 304	0	1.1×10^3	7.30×10^5	12.6×10^{-6}	0.87	3.65×10^8	1.44×10^{-7}	0.62	3.66×10^5
	168	4.4×10^3	5.15×10^7	7.41×10^{-6}	0.92	7.47×10^3	2.55×10^{-6}	0.56	5.15×10^7
Citric Acid TiAlTaZ-rNbN	0	3.6×10^3	1.76×10^7	5.18×10^{-6}	0.91	2.67×10^7	2.40×10^{-2}	0.53	4.43×10^7
	168	4.5×10^3	5.48×10^7	3.97×10^{-6}	0.92	1.07×10^7	2.62×10^{-2}	0.53	6.55×10^7
Tap water AISI 304	0	2.8×10^3	2.99×10^5	2.52×10^{-6}	0.90	1.64×10^7	5.45×10^{-7}	0.58	1.67×10^7
	168	13.5×10^3	4.06×10^6	1.93×10^{-6}	0.90	1.40×10^8	2.39×10^{-7}	0.64	1.44×10^8
Tap water TiAlTaZrNbN	0	28.1×10^3	5.85×10^6	5.58×10^{-6}	0.90	1.28×10^7	1.84×10^{-9}	0.65	1.87×10^7
	168	36.1×10^3	1.22×10^6	3.93×10^{-6}	0.92	7.03×10^7	3.43×10^{-8}	0.59	7.16×10^7
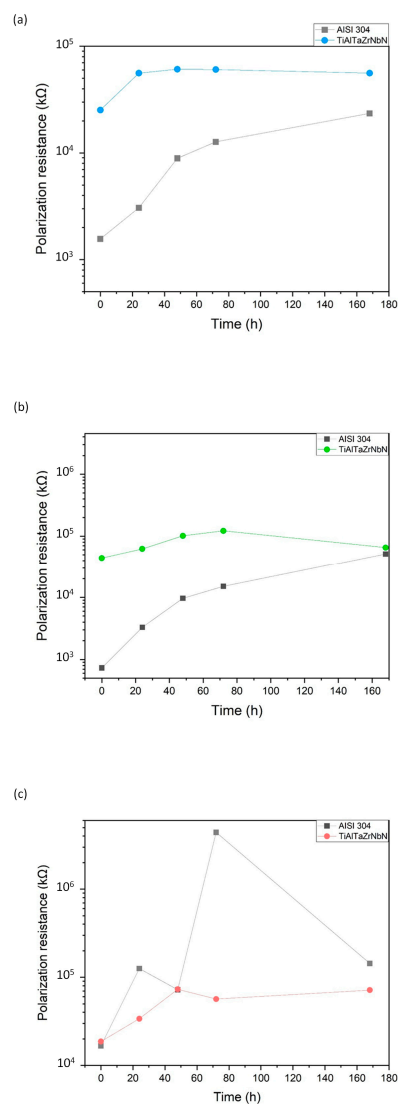
Figure 4. Polarization resistance (Rp) of the AISI 304 substrate and the TiAlTaZrNbN coating in (**a**) acetic acid solution; (**b**) citric acid solution; and (**c**) tap water.

Regarding the polarization resistance for the tap-water solution, the measurement for the substrate progressively increases in value, while in the case of the coating, it remains constant over time at the order of 10^{-7}. This behavior is shown in Figure 5c, where the substrate registers higher polarization resistance values, indicating strong protection against the electrolyte. The increase in Rp observed in both curves from 0 h to 72 h is attributed to corrosion products that block the pores and increase the resistive path [33]. In other words, as the polarization resistance increases, the porosity decreases.
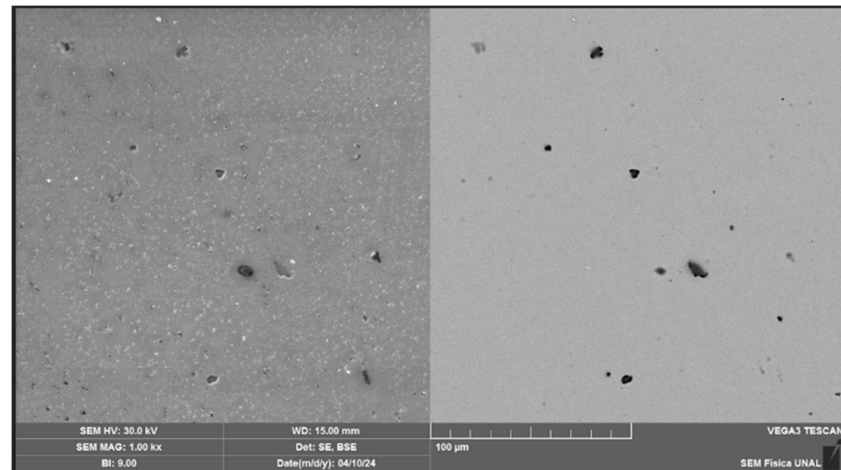
(a)
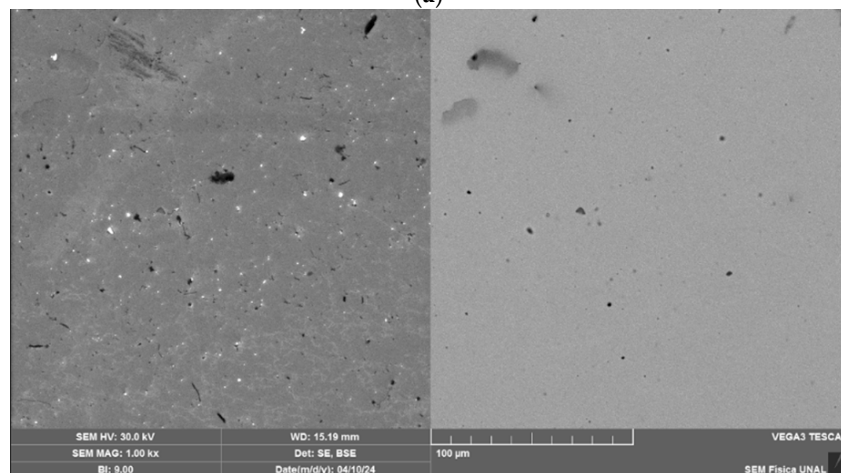
(b)
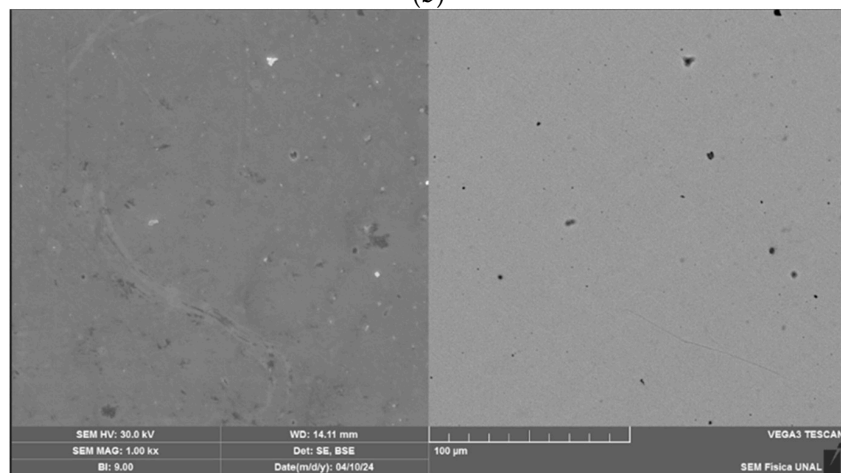
(c)

Figure 5. SEM images of the TiAlTaZrNbN coating on AISI 304 substrate at $1000\times$ and surface roughness measurement images after EIS analysis in (**a**) acetic acid; (**b**) citric acid; and (**c**) tap water.

To verify whether any changes occurred in the elements after the EIS analysis, the chemical composition of the coating on the substrate was also measured. The results suggest that no significant change in composition occurred. Although the film shows the presence of some pores, SEM and roughness analyses demonstrate that it continues to provide effective protection to the AISI 304 substrate against corrosion, as shown in Figure 5.

3.4. Corrosion Mechanisms

3.4.1. Acetic Acid

According to the EIS analysis, it can be determined that the surface film is the main element controlling the corrosion process. Its resistance will determine the corrosion performance, and it is likely that corrosion occurs at defects in the coating. In this case, the electrolyte (CH_3COOH solution in distilled water) dissociates into CH_3COO^- and H^+. The reaction is reversible, so the final concentration of acetic acid and acetate ions will depend on the pH of the solution. Near the corrosion potential, metal dissolution reactions occur along with two cathodic reactions corresponding to the reduction of hydrogen ions and undissociated acetic acid [34–36]. It is concluded that acetic acid is not an electroactive species but rather acts as a proton-generating source at the metal surface (acetic acid dissociation reaction).

The proposed corrosion mechanism for the coating–substrate system involves the diffusion of the electrolyte towards the AISI 304 substrate through the defects found (pores or cracks) in the coating. The corrosion reactions are related to the contact between the electrolyte anions and the metal ions of the substrate. Electrochemical studies show that cathodic reactions occur on the surface of the film, while anodic reactions take place on the substrate surface [37]. These can be described by the following reactions: the anodic reaction (3) and the cathodic reaction (4).

$$M - ne \rightarrow M^{n+} \tag{3}$$

$$O_2 + 2H_2O + 4e \rightarrow 4OH^- \tag{4}$$

3.4.2. Citric Acid

Citric acid is one of the food simulants suggested in the European directive for testing metals and alloys used in contact with food. During the test with this electrolyte, the hydrogen evolution reaction is also expected to occur rapidly as the main reaction, along with the oxygen reduction reaction. According to studies, the activity and diffusion/migration rate of hydrogen ions are much higher than those of oxygen molecules [38]. Furthermore, the growth and stability of the passive films generated on the surface will be regulated by the chemical composition of the alloy and the pH of the aqueous environment.

It is also defined that citric acid is a weak acid and can partially ionize to H^+ and three anionic ions in an aqueous solution $H_2C_6H_5O_7^-$, $HC_6H_5O_7^{2-}$, and $HC_6H_5O_7^{3-}$ [39]. Exposures to citric acid initially increase the release of metals from stainless steels but result in greater surface passivation and a reduction in metal release over time due to chromium enrichment in the passive oxide layer [40]. The mechanism will also depend on the adsorption of the ligand, its ability to form stable complexes, and the kinetics of the complex detachment from the surface into solution [41,42]. Based on this, and as reported with acetic acid, the corrosion mechanism proposed involves the diffusion of the electrolyte to the AISI 304 substrate through defects (pores or cracks) in the coating. Corrosion reactions are related to the contact between the electrolyte anions and the metal ions of the substrate.

3.4.3. Tap Water

In this case, the corrosion mechanism is also proposed as the diffusion of the electrolyte toward the AISI 304 substrate through defects found in the deposited film. On one hand, tap water typically has a neutral pH between seven and eight. On the other hand, the general corrosion process of steel involves a coupled electrochemical reaction consisting of the anodic oxidation of the metal and the cathodic reduction of oxygen. Regarding the latter, the reaction current is limited by the diffusion of oxygen [43]. In the case of anodic oxidation, the proposed corrosion mechanism of steel initially produces water-soluble Fe^{2+}, and then, the oxidized metal ions react with hydroxide ions to form a mixture of hydrated iron oxides. Unlike the previously studied media, in this case, there is no dissociation of any acid, but rather a reaction caused by the contact of oxygen and hydrogen atoms with the elements of the alloy and the substrate.

From the analysis of the corrosion mechanisms, it is concluded that transition metal nitrides are electrochemically inert, which gives them a high polarization resistance [44]. This was confirmed in the analyzed coating, which showed a more positive corrosion potential and a lower corrosion current, indicating an improvement in the corrosion resistance of the substrate. It is observed that the addition of the high-entropy alloy coating significantly improves the corrosion resistance of the AISI 304 substrate in acetic acid and citric acid solutions (food simulants with pH $\leq$ 4.5).

This increase in corrosion resistance is due to the formation of a passivation layer and an oxide layer, which are influenced by the internal diffusion of oxygen and the external diffusion of metal atoms [45]. This process is affected by the Gibbs free energy of the oxides and the electronegativity of the metal elements, as metals with lower electronegativity react more easily with oxygen [46].

3.4.4. Proposed Mechanism of Corrosion

Figure 6 presents a schematic illustration of the possible mechanisms occurring in the coatings as a function of the three electrolytes used. The proposed corrosion mechanism for the coating–substrate system involves the diffusion of the electrolyte toward the AISI 304 substrate through defects (such as pores or cracks) present in the coating. The corrosion reactions are associated with the interaction between the anions from the electrolyte and the metallic ions of the substrate. Electrochemical studies indicate that cathodic reactions occur on the surface of the film, while anodic reactions take place at the substrate surface [37].
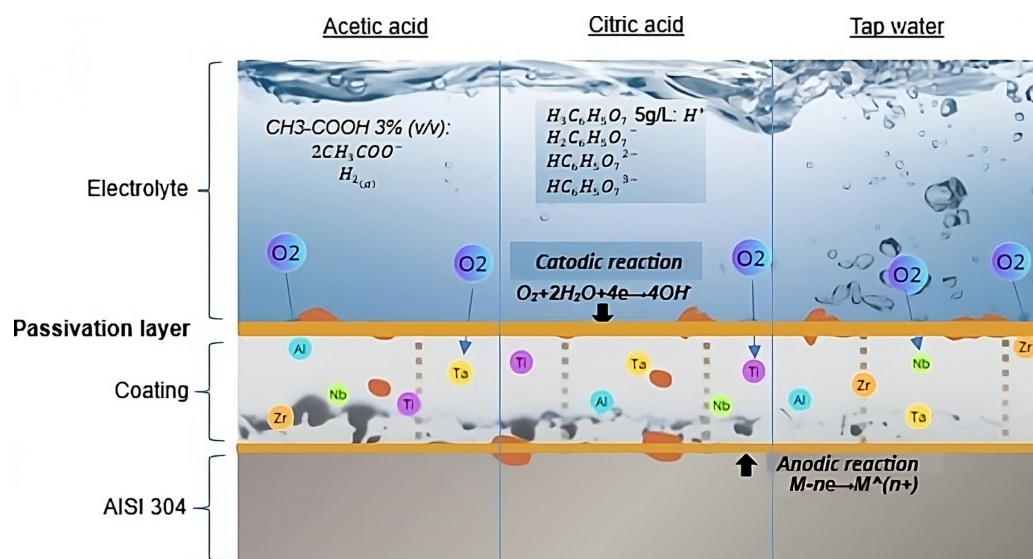

Figure 6. Proposed corrosion mechanism for acetic acid solution, citric acid solution, and tap water.

Since the corrosion process occurs through the pores or microcracks of the deposited coating, the ions generated by the anodic reaction combine with the OH^- products resulting from the cathodic reaction. This process can be described by the reaction (5):

$$M^{n+} + nH_2O \rightarrow M(OH)_n + nH^+ \tag{5}$$

In the case of a 3% CH_3COOH electrolyte, the acid dissociates according to the reaction (6):

$$CH_3COOH \leftrightarrow CH_3COO^- + H^+ \tag{6}$$
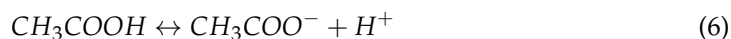
This reaction is reversible, so the final concentration of acetic acid and acetate ions will depend upon the pH of the solution. Near the corrosion potential, the dissolution reactions of metals ($Fe^{2+}_{(aq)}$, $Ni^{2+}_{(aq)}$, $Cr^{3+}_{(aq)}$) occur alongside two cathodic reactions corresponding to the reduction of hydrogen ions and undissociated acetic acid, as shown in the following reactions (7) and (8) [34–36]:

$$2H^+_{(aq)} + 2e^- \leftrightarrow H_{2_{(g)}} \tag{7}$$

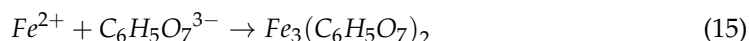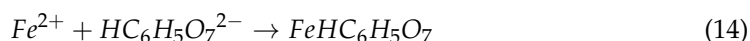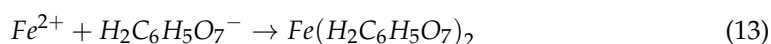$$2CH_3COOH_{(aq)} + 2e^- \leftrightarrow H_2 + 2CH_3COO^- \tag{8}$$
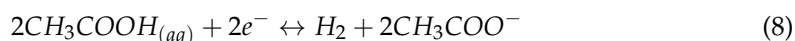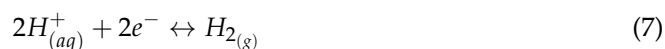
It is known that acetic acid is not an electroactive species but acts as a source of protons at the metal surface (acetic acid dissolution reaction). Zhang et al. described how the elements may interact with the electrolyte. They studied the behavior of aluminum in acetic acid, asserting that the corrosion process occurs via a chemical transition reaction, in which the H^+ in the solution is adsorbed at the active center of the aluminum surface, converting the hydrogen ion into a hydrogen atom. The hydrogen atom then forms a corrosion product on the surface and is subsequently desorbed into the solution [35].
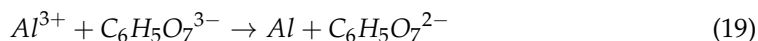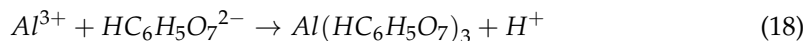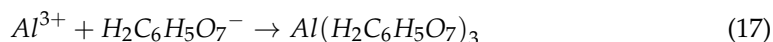
On the other hand, citric acid is a strong metal-complexing agent, capable of forming metal complexes with metals in solution or with surface oxide metals, depending on the strength of these complexes and their bonds, which determines their detachment from the surface. According to Mazinanian et al., citric acid has a greater capacity to generate such complexes compared to acetic acid, resulting in a more rapid passivation (chromium enrichment) of the surface oxide layer [16]. Citric acid is also known to be a weak acid and can partially ionize in aqueous solution to produce H^+ and three anionic species: $H_2C_6H_5O_7^-$, $HC_6H_5O_7^{2-}$ y $HC_6H_5O_7^{3-}$. Their formation is explained by the reactions (9)–(11) [47]:

$$H_3C_6H_5O_7 \leftrightarrow H^+ + H_2C_6H_5O_7^- \tag{9}$$

$$H_2C_6H_5O_7^- \leftrightarrow H^{++} + HC_6H_5O_7^{2-} \tag{10}$$

$$HC_6H_5O_7^{2-} \leftrightarrow H^+ + HC_6H_5O_7^{3-} \tag{11}$$
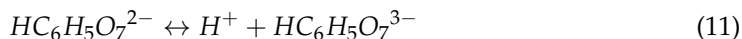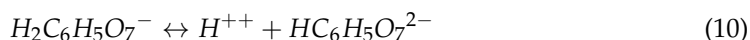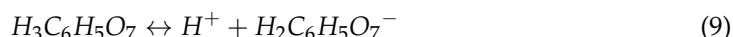
The anodic dissolution of the surface can be expressed by the following reaction. The Fe^{2+} product reacts with the acid anions as shown below (12)–(15) [39]:

$$Fe \rightarrow Fe^{2+} + 2e^- \tag{12}$$

$$Fe^{2+} + H_2C_6H_5O_7^- \rightarrow Fe(H_2C_6H_5O_7)_2 \tag{13}$$

$$Fe^{2+} + HC_6H_5O_7^{2-} \rightarrow FeHC_6H_5O_7 \tag{14}$$

$$Fe^{2+} + C_6H_5O_7^{3-} \rightarrow Fe_3(C_6H_5O_7)_2 \tag{15}$$

An example of how the anionic species react with the alloy elements can be illustrated with the transition metals in the coating. For instance, with aluminum in the coating, the reactions (16)–(19) may occur:

$$Al \rightarrow Al^{3+} + 3e^- \tag{16}$$

$$Al^{3+} + H_2C_6H_5O_7^- \rightarrow Al(H_2C_6H_5O_7)_3 \tag{17}$$

$$Al^{3+} + HC_6H_5O_7^{2-} \rightarrow Al(HC_6H_5O_7)_3 + H^+ \tag{18}$$

$$Al^{3+} + C_6H_5O_7^{3-} \rightarrow Al + C_6H_5O_7^{2-} \tag{19}$$

Exposure to citric acid initially increases the release of metals from stainless steels but ultimately results in greater surface passivation and a reduction in metal release over time due to chromium enrichment in the passive oxide layer [40]. The mechanism also depends on the adsorption of the ligand (complexing agent), its ability to form stable complexes, and the kinetics of complex detachment from the surface into solution [42,47].

Finally, in the presence of water as the electrolyte, it is expected that iron and chromium from the substrate will dissolve as $Fe^{2+}_{(aq)}$ and $Cr^{2+}_{(aq)}$, with the latter potentially being further oxidized to $Cr^{3+}_{(aq)}$ [48]. The coating–substrate system did not show significant improvement compared to the substrate alone, suggesting that this corrosive medium is not a severe corrosion agent for the material produced. Tap water typically has a neutral pH between seven and eight. Moreover, the general corrosion process of steel occurs via a coupled electrochemical reaction consisting of the anodic oxidation of the metal and the cathodic reduction of the oxygen.

4. Conclusions

The (TiAlZrTaNb)N$_x$ coatings deposited on AISI 304 stainless steel exhibited a face-centered cubic (FCC) crystal structure with a preferential orientation along the (111) plane, a lattice parameter of 0.4526 nm, and an average crystallite size of 18.20 nm. The coatings demonstrated a near-equiatomic composition, with average elemental concentrations of Ti (23.79%), Nb (23.38%), Zr (19.09%), Al (17.50%), and Ta (16.24%). SEM and three-dimensional optical microscopy analyses revealed that the coatings formed dense, homogeneous layers with low surface roughness and a minimal concentration of micropores.

Electrochemical testing in food-simulant electrolytes confirmed the superior anticorrosive performance of the coatings. In particular, the coatings achieved corrosion protection efficiencies exceeding 98% in acetic acid and citric acid solutions (representative of food environments with pH $\leq$ 4.5). EIS results confirmed enhanced electrochemical stability and barrier properties of the coating compared to bare 304 stainless steel.

This enhancement is attributed to the formation of stable passivation layers comprised of oxides from the constituent alloying elements, as well as the inhibitory effect of weak acids. In contrast, tests conducted in tap water (simulating aqueous, alcoholic, and fatty-food environments) showed no significant improvement in corrosion resistance compared to the uncoated substrate.

In summary, the (TiAlZrTaNb)N$_x$ high-entropy alloy coatings significantly enhance the corrosion resistance of AISI 304 stainless steel in acidic food-simulant environments. These findings highlight the potential of such coatings to improve the durability and service life of materials and utensils intended for use in the food industry.

Author Contributions: Conceptualization, O.P. and J.O.; Methodology, M.-C.C.; O.P. and J.O.; Investigation, M.-C.C.; O.P. and J.O.; Writing – original draft, M.-C.C. and J.O.; Writing – review and editing, M.-C.C.; O.P. and J.O.; Project administration, O.P.; Funding acquisition, O.P. and J.O. All authors have read and agreed to the published version of the manuscript.

Conflicts of Interest: The authors declare no conflicts of interest. The funders had no role in the design of the study; in the collection, analyses, or interpretation of data; in the writing of the manuscript; or in the decision to publish the results.

Abbreviations

The following abbreviations are used in this manuscript:

HEA	High-Entropy Alloy
HiPIMS	High-Power Impulse Magnetron Sputtering
PVD	Physical Vapor Deposition

References

1. Zhou, H.; Jiang, L.; Jia, L.; Zhu, S.; Wang, L.; Wu, A.; Zhang, X. Interstitial boron-doped FeCoNiCr high entropy alloys with excellent electromagnetic-wave absorption and resistance to harsh environments. *J. Alloys Compd.* **2023**, *959*, 170579. [CrossRef]
2. Braic, V.; Vladescu, A.; Balaceanu, M.; Luculescu, C.R.; Braic, M. Nanostructured multi-element (TiZrNbHfTa) N and (TiZrNbHfTa) C hard coatings. *Surf. Coat. Technol.* **2012**, *211*, 117–121. [CrossRef]
3. Bachani, S.K.; Wang, C.-J.; Lou, B.-S.; Chang, L.-C.; Lee, J.-W. Fabrication of TiZrNbTaFeN high-entropy alloys coatings by HiPIMS: Effect of nitrogen flow rate on the microstructural development, mechanical and tribological performance, electrical properties and corrosion characteristics. *J. Alloys Compd.* **2021**, *873*, 159605. [CrossRef]
4. APogrebnjak, D.; Beresnev, V.M.; Smyrnova, K.V.; Kravchenko, Y.O.; Zukowski, P.V.; Bondarenko, G.G. The influence of nitrogen pressure on the fabrication of the two-phase superhard nanocomposite (TiZrNbAlYCr) N coatings. *Mater. Lett.* **2018**, *211*, 316–318. [CrossRef]
5. Miracle, D.B.; Senkov, O.N. A critical review of high entropy alloys and related concepts. *Acta Mater.* **2017**, *122*, 448–511.
6. Pshyk, A.V.; Vasylenko, A.; Bakhit, B.; Hultman, L.; Schweizer, P.; Edwards, T.E.J.; Michler, J.; Greczynski, G. High-entropy transition metal nitride thin films alloyed with Al: Microstructure, phase composition and mechanical properties. *Mater. Des.* **2022**, *219*, 110798.
7. Yuan, M.; Gao, X.; Gu, X.; Dong, C.; Wang, S.; Wen, M.; Zhang, K. Simultaneous enhancement of hardness and wear and corrosion resistance of high-entropy transition-metal nitride. *J. Am. Ceram. Soc.* **2023**, *106*, 1356–1368.
8. Lou, B.-S.; Lin, Y.-C.; Lee, J.-W. Mechanical Properties and Corrosion Resistance of AlCrNbSiTiN High Entropy Alloy Nitride Coatings. *Coatings* **2023**, *13*, 1724. [CrossRef]
9. Arshad, M.; Amer, M.; Hayat, Q.; Janik, V.; Zhang, X.; Moradi, M.; Bai, M. High-Entropy Coatings (HEC) for High-Temperature Applications: Materials, Processing, and Properties. *Coatings* **2022**, *12*, 691. [CrossRef]
10. Shu, R.; Paschalidou, E.-M.; Rao, S.G.; Bakhit, B.; Boyd, R.; Moro, M.V.; Primetzhofer, D.; Greczynski, G.; Nyholm, L.; le Febvrier, A.; et al. Effect of nitrogen content on microstructure and corrosion resistance of sputter-deposited multicomponent (TiNbZrTa) Nx films. *Surf. Coat. Technol.* **2020**, *404*, 126485. [CrossRef]
11. Tian, C.; Cai, H.; Xue, Y. Effect of Working Pressure on Tribological Properties of Ce-Ti/MoS2 Coatings Using Magnetron Sputter. *Coatings* **2022**, *12*, 1576. [CrossRef]
12. Ehiasarian, A. High-power impulse magnetron sputtering and its applications. *Pure Appl. Chem.* **2010**, *82*, 1247–1258. [CrossRef]
13. Lundin, D. The HiPIMS Process. 2010. Available online: https://urn.kb.se/resolve?urn=urn:nbn:se:liu:diva-56748 (accessed on 24 June 2024).
14. Dias, N.F.L.; Meijer, A.L.; Biermann, D.; Tillmann, W. Structure and mechanical properties of TiAlTaN thin films deposited by dcMS, HiPIMS, and hybrid dcMS/HiPIMS. *Surf. Coat. Technol.* **2024**, *487*, 130987. [CrossRef]
15. Samuelsson, M.; Lundin, D.; Jensen, J.; Raadu, M.A.; Gudmundsson, J.T.; Helmersson, U. On the film density using high power impulse magnetron sputtering. *Surf. Coat. Technol.* **2010**, *205*, 591–596.

16. Mazinanian, N.; Wallinder, I.O.; Hedberg, Y. Comparison of the influence of citric acid and acetic acid as simulant for acidic food on the release of alloy constituents from stainless steel AISI 201. *J. Food Eng.* **2015**, *145*, 51–63. [CrossRef]

17. Sputtering Yields. Available online: https://www.angstromsciences.com/sputtering-yields (accessed on 26 June 2024).

18. Ren, B.; Yan, S.Q.; Zhao, R.F.; Liu, Z.X. Structure and properties of (AlCrMoNiTi) Nx and (AlCrMoZrTi) Nx films by reactive RF sputtering. *Surf. Coat. Technol.* **2013**, *235*, 764–772. [CrossRef]

19. Yeh, J.-W. Alloy Design Strategies and Future Trends in High-Entropy Alloys. *JOM* **2013**, *65*, 1759–1771. [CrossRef]

20. Huaizhi, Q.; Minglong, G.; Dongdong, Z.; Wenda, S.; Fengfang, L.; Jing, B.; Qiuzhi, G.; Xiang, Z. Effect of heat treatment time on the microstructure and properties of FeCoNiCuTi high-entropy alloy. *J. Mater. Res. Technol.* **2023**, *24*, 4510–4516. [CrossRef]

21. Tsai, M.-H.; Yeh, J.-W. High-Entropy Alloys: A Critical Review. *Mater. Res. Lett.* **2014**, *2*, 107–123. [CrossRef]

22. Karimzadeh, M.; Malekan, M.; Mirzadeh, H.; Li, L.; Saini, N. Effects of titanium addition on the microstructure and mechanical properties of quaternary CoCrFeNi high entropy alloy. *Mater. Sci. Eng. A* **2022**, *856*, 143971. [CrossRef]

23. Miletić, A.; Panjan, P.; Škorić, B.; Čekada, M.; Dražič, G.; Kovač, J. Microstructure and mechanical properties of nanostructured Ti–Al–Si–N coatings deposited by magnetron sputtering. *Surf. Coat. Technol.* **2014**, *241*, 105–111. [CrossRef]

24. Kaciulis, S.; Mezzi, A.; Montesperelli, G.; Lamastra, F.; Rapone, M.; Casadei, F.; Valente, T.; Gusmano, G. Multi-technique study of corrosion resistant CrN/Cr/CrN and CrN: C coatings. *Surf. Coat. Technol.* **2006**, *201*, 313–319.

25. Cheng, K.-H.; Lai, C.-H.; Lin, S.-J.; Yeh, J.-W. Structural and mechanical properties of multi-element (AlCrMoTaTiZr)Nx coatings by reactive magnetron sputtering. *Thin Solid Film.* **2011**, *519*, 3185–3190. [CrossRef]

26. Mendez, A.; Monclus, M.; Santiago, J.; Fernandez-Martinez, I.; Rojas, T.; Garcia-Molleja, J.; Avella, M.; Dams, N.; Panizo-Laiz, M.; Molina-Aldareguia, J. Effect of Al content on the hardness and thermal stability study of AlTiN and AlTiBN coatings deposited by HiPIMS. *Surf. Coat. Technol.* **2021**, *422*, 127513. [CrossRef]

27. Wu, X.; Xu, X.; Jiang, Y.; Chen, C.; Han, H.; Zhao, L.; Xu, J.; Yu, L. Nitriding high entropy alloy films: Opportunities and challenges. *Surf. Coat. Technol.* **2024**, *476*, 130157.

28. Kumar, A.; Malik, G.; Chandra, R.; Mulik, R.S. Sputter-grown hierarchical nitride (TiN & h-BN) coatings on BN nanoplates reinforced Al7079 alloy with improved corrosion resistance. *Surf. Coat. Technol.* **2022**, *432*, 128061. [CrossRef]

29. Wetzel, A.; von der Au, M.; Dietrich, P.M.; Radnik, J.; Ozcan, O.; Witt, J. The comparison of the corrosion behavior of the CrCoNi medium entropy alloy and CrMnFeCoNi high entropy alloy. *Appl. Surf. Sci.* **2022**, *601*, 154171. [CrossRef]

30. Ahmed, M.K.; Shahid, M.; Khan, Z.A.; Ammar, A.U.; Saboor, A.; Khalid, A.; Hayat, A.; Saeed, A.; Koohgilani, M. Electrochemical comparison of SAN/PANI/FLG and ZnO/GO coated cast iron subject to corrosive environments. *Materials* **2018**, *11*, 2239.

31. Berríos, J.C. ▷ Propiedades dieléctricas de los materiales aislantes (fórmula y constante) | TELCOM® 2024. TELCOM: Aprenda ingeniería eléctrica y electrónica (gratis). Available online: https://telcomplus.org/propiedades-dielectricas-del-aislamiento/ (accessed on 20 July 2024).

32. Song, G.L.; Liu, M. Corrosion and electrochemical evaluation of an Al–Si–Cu aluminum alloy in ethanol solutions. *Corrosion Science* **2013**, *72*, 73–81.

33. González-Hernández, A.; Morales-Cepeda, A.B.; Flores, M.; Caicedo, J.C.; Aperador, W.; Amaya, C. Electrochemical Properties of TiWN/TiWC Multilayer Coatings Deposited by RF-Magnetron Sputtering on AISI 1060. *Coatings* **2021**, *11*, 797. [CrossRef]

34. Zuñiga-Diaz, K.; Arrieta-Gonzalez, C.D.; Porcayo-Calderon, J.; Gonzalez-Rodriguez, J.G.; Casales-Diaz, M.; Martinez-Gomez, L. Electrochemical Behavior of Austenitic Stainless Steels Exposed to Acetic Acid Solution. *Int. J. Electrochem. Sci.* **2020**, *15*, 1242–1263. [CrossRef]

35. Zhang, P.; Zhang, H.; Xu, Y.; Li, H.; Liu, J.; Fan, Y.; Wang, S. Corrosion Behavior of Aluminum in Dilute Acetic Acid Solution Simulating Cooling Water in HVDC Transmission. *Int. J. Electrochem. Sci.* **2022**, *17*, 220324. [CrossRef]

36. Singh, S.K.; Mukherjee, A.K. Kinetics of Mild Steel Corrosion in Aqueous Acetic Acid Solutions. *J. Mater. Sci. Technol.* **2010**, *26*, 264–269. [CrossRef]

37. Moreno Amado, M. Resistencia a la corrosión y al desgaste de recubrimientos nanoestructurados de Zirconia (ZrO$_2$)—Plata (Ag) y/o Alúmina (Al$_2$O$_3$) obtenidos con técnica de "Sputtering" reactivo con magnetrón desbalanceado. June 2019. Available online: https://repositorio.unal.edu.co/handle/unal/78428 (accessed on 25 July 2024).

38. Shahidi, M.; Gholamhosseinzadeh, M.R. Electrochemical evaluation of AA6061 aluminum alloy corrosion in citric acid solution without and with chloride ions. *J. Electroanal. Chem.* **2015**, *757*, 8–17. [CrossRef]

39. Li, X.; Deng, S. Ce(SO4)2 as an efficient corrosion inhibitor for cold rolled steel in citric acid solution. *J. Taiwan Inst. Chem. Eng.* **2021**, *122*, 273–283. [CrossRef]

40. Mazinanian, N.; Herting, G.; Odnevall, I.; Hedberg, Y. Metal Release and Corrosion Resistance of Different Stainless Steel Grades in Simulated Food Contact. *Corrosion* **2016**, *72*, 775–790. [CrossRef]

41. Mazinanian, N.; Wallinder, I.O.; Hedberg, Y.S. Influence of citric acid on the metal release of stainless steels. *Corros. Sci. Technol.* **2015**, *14*, 166–171.

42. Mazinanian, N.; Hedberg, Y.S. Metal Release Mechanisms for Passive Stainless Steel in Citric Acid at Weakly Acidic pH. *J. Electrochem. Soc.* **2016**, *163*, C686. [CrossRef]

43. Vasyliev, G.S. The influence of flow rate on corrosion of mild steel in hot tap water. *Corros. Sci.* **2015**, *98*, 33–39.

44. Grips, V.K.W.; Selvi, V.E.; Barshilia, H.C.; Rajam, K.S. Effect of electroless nickel interlayer on the electrochemical behavior of single layer CrN, TiN, TiAlN coatings and nanolayered TiAlN/CrN multilayer coatings prepared by reactive dc magnetron sputtering. *Electrochim. Acta* **2006**, *51*, 3461–3468. [CrossRef]

45. Yang, J.; Zhang, F.; Chen, Q.; Zhang, W.; Zhu, C.; Deng, J.; Zhong, Y.; Liao, J.; Yang, Y.; Liu, N.; et al. Effect of Au-ions irradiation on mechanical and LBE corrosion properties of amorphous AlCrFeMoTi HEA coating: Enhanced or deteriorated? *Corros. Sci.* **2021**, *192*, 109862. [CrossRef]

46. Zhang, Z.; Han, E.-H.; Xiang, C. Effect of helium ion irradiation on short-time corrosion behavior of two novel high-entropy alloys in simulated PWR primary water. *Corros. Sci.* **2021**, *191*, 109742. [CrossRef]

47. Influence of Citric Acid on the Metal Release of Stainless Steels-Corrosion Science and Technology | Korea Science. Available online: https://koreascience.or.kr/article/JAKO201528551642095.page (accessed on 11 August 2024).

48. Lodhi, M.J.K.; Deen, K.M.; Haider, W. Corrosion behavior of additively manufactured 316L stainless steel in acidic media. *Materialia* **2018**, *2*, 111–121. [CrossRef]